



HAL
open science

Effect of the 2018 Martian global dust storm on the CO₂ density in the lower nightside thermosphere observed from MAVEN/IUVS Lyman-alpha absorption

Jean-Yves Chaufray, M. Chaffin, Justin Deighan, S. Jain, N. Schneider, M. Mayyasi, B. Jakosky

► To cite this version:

Jean-Yves Chaufray, M. Chaffin, Justin Deighan, S. Jain, N. Schneider, et al.. Effect of the 2018 Martian global dust storm on the CO₂ density in the lower nightside thermosphere observed from MAVEN/IUVS Lyman-alpha absorption. *Geophysical Research Letters*, 2020, 47 (7), pp.e2019GL082889. 10.1029/2019GL082889 . insu-02158439

HAL Id: insu-02158439

<https://insu.hal.science/insu-02158439v1>

Submitted on 16 Dec 2020

HAL is a multi-disciplinary open access archive for the deposit and dissemination of scientific research documents, whether they are published or not. The documents may come from teaching and research institutions in France or abroad, or from public or private research centers.

L'archive ouverte pluridisciplinaire **HAL**, est destinée au dépôt et à la diffusion de documents scientifiques de niveau recherche, publiés ou non, émanant des établissements d'enseignement et de recherche français ou étrangers, des laboratoires publics ou privés.

1 **Effect of the 2018 Martian global dust storm on the CO₂ density in the lower nightside**
2 **thermosphere observed from MAVEN/IUVS Lyman-alpha absorption**

3
4 J-Y. Chaufray¹, M. Chaffin², J. Deighan², S. Jain², N. Schneider², M. Mayyasi³, and B. Jakosky²

5 ¹ LATMOS/IPSL, CNRS, UVSQ Université Paris-Saclay, Sorbonne Université, Guyancourt, France

6 ²LASP, University of Colorado Boulder, Boulder, Colorado, USA

7 ³Center for Space Physics, Boston University, Boston, Massachusetts, USA

8
9
10 **Abstract**

11 The MAVEN/IUVS instrument measures Lyman- α emissions from interplanetary and martian
12 hydrogen at the limb and through the extended corona of Mars. In June 2018, a Global Dust
13 Storm (GDS) surrounded Mars for a few months, heating the lower atmosphere and leading to an
14 expansion of the Martian atmosphere. Nightside IUVS observations before and throughout this
15 GDS showed the altitude of CO₂ absorption of Lyman- α photons in the thermosphere to increase
16 by 4.5 ± 1.0 km on 8 June 2018. This shift is attributed to an increase of the CO₂ density by a
17 factor 1.9 ± 0.2 at 110 km due to the heating of the lower atmosphere. These nightside
18 observations, not previously used to study dust storms, in an altitude range not sampled by other
19 instruments, are consistent with dayside MAVEN observations and allow for more
20 comprehensive determination of the global changes produced by the GDS on the Martian
21 thermosphere.

22
23
24
25

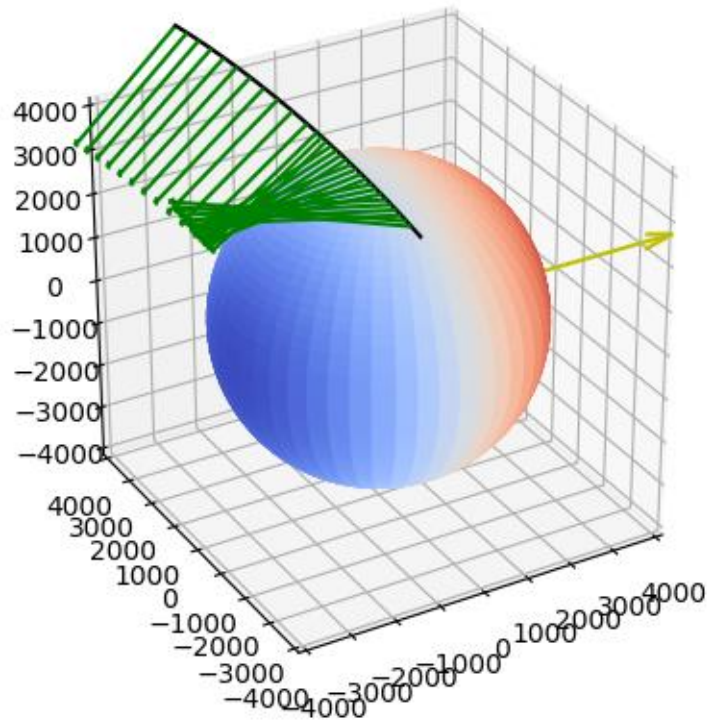
26 **1) Introduction**

27 Absorption of UV photons in the Martian upper atmosphere is the main source of thermospheric
28 heating as well as of ionization, dissociation and excitation of CO₂ molecules (e.g. Fox et al.
29 2008). The partial absorption of the UV solar or stellar photons can also be used by remote
30 sensing instrument to derive the density, temperature or composition of the Martian thermosphere
31 as done by Mars Express/SPICAM (e.g. Forget et al. 2009) and more recently by MAVEN/IUVS
32 (Gröller et al. 2015, 2018). Another method used to derive the CO₂ density in the Martian
33 nightside thermosphere near 110 km utilizes the absorption by CO₂ of Lyman- α photons emitted
34 in the interplanetary medium and Martian exosphere (Bertaux et al. 2005, Chaufray et al. 2011).
35 Chaufray et al. (2011) used this method to derive seasonal variations of lower thermospheric
36 nightside CO₂ density that were in good agreement with variations deduced from stellar
37 occultations. This method was shown to be less accurate than the stellar/solar occultation method
38 because it is based on only one wavelength instead of the full UV spectral range for occultations,
39 yet it has the advantage of simplicity due to requiring fewer constraints on pointing, and
40 portability to any latitudes, longitudes, and local time at nightside compared with terminator-
41 limited solar occultations. In June 2018, an intense Global Dust Storm (GDS) surrounded Mars
42 lasting a few months, heating the lower atmosphere (Kass et al. 2018) and led to an expansion of
43 the Martian atmosphere by few kilometers at thermospheric altitudes (Bougher et al., 2019, see
44 also Jain et al. this issue, and Elrod et al this issue). Since Lyman- α absorption occurs in the
45 lower thermosphere, an increase of CO₂ density at a given altitude during the GDS would be
46 expected to increase the altitude of Lyman- α absorption by CO₂. In this paper, MAVEN/IUVS
47 nightside “limb scans” are used to estimate the increase of the CO₂ density at 110 km produced
48 by this GDS. Section 2 describes the dataset and assumptions used to derive the CO₂ density. In

49 section 3 the variations of CO₂ density at 110 km during the dust storm are shown. The results are
50 compared to dayside variations observed by other instruments in section 4.

51 **2) Data analysis**

52 At the beginning of the global dust storm, the MAVEN spacecraft periapsis was on the dayside,
53 and its apoapsis on the nightside. The IUVS “coronal scans” occur on the inbound and outbound
54 segments of the orbit from periapsis (McClintock et al. 2015). During these parts of MAVEN’s
55 orbit, the Lyman- α emission of atomic hydrogen is observed scanning the limb with tangent
56 altitudes ranging from below the planet’s surface up to the exosphere \sim 3400 km. During the
57 outbound leg, the spacecraft was partly in the dayside on 8 June 2018 and in the nightside during
58 the inbound leg. In this paper, the nightside inbound observations from MAVEN/IUVS where the
59 solar zenith angle of the tangent point is larger than $\sim 90^\circ$ and the solar zenith angle of the
60 spacecraft is larger than 90° are used. The geometry of one observation is displayed on Fig. 1



61

62 *Figure.1 Geometry of the observation during orbit 7178 in the Mars Sun Orbit (MSO) frame. All*
 63 *axis are in km. The Martian surface is red at the dayside and blue at the nightside. MAVEN is*
 64 *moving toward is pericenter and its position during the observation is represented by the black*
 65 *solid line. The lines of sight of IUVS during the different inlimb scans are represented in green.*
 66 *The sun direction is shown by the yellow arrow (X axis).*

67

68 Atmospheric hydrogen is not directly illuminated by the Sun in the shadow, and the brightness
 69 dispersion at a given tangent altitudes is smaller on the nightside than on the dayside, making the
 70 CO₂ density retrieval easier. In this study, we only use observations with a tangent altitude
 71 spanning the surface to 250 km (files tagged “inlimb” in the Planetary Data System archives).
 72 The resulting observations include 33 non-consecutive orbits spanning orbit # 7106 (25 May

73 2018) to orbit # 7256 (22 June 2018). Six inbound limb scans are done in each orbit with a
74 sampling of approximately 10 km. 7 spatial bins are transmitted per limb scan, leading to 42
75 individual limb profiles per orbit. The latitude, longitude, SZA and local time ranges at the
76 tangent point covered for each orbit are given in Table 1

# Orbit	Day	Ls	SZA	Latitude	E Longitude	Local Time
7106	25 May	181.5	117-138	27-55	49-74	20.8-22.7
7112	26 May	182.2	117-138	29-55	17-42	20.8-22.6
7116	27 May	182.6	117-137	30-54	115-140	20.6-22.5
7120	27 May	183.0	118-137	26-54	215-239	20.5-22.4
7124	28 May	183.5	118-137	26-53	313-338	20.4-22.3
7128	29 May	183.9	118-136	25-53	52-76	20.4-22.2
7132	30 May	184.3	118-136	24-52	151-174	20.3-22.1
7136	30 May	184.7	118-135	23-52	250-273	20.2-22.1
7140	31 May	185.1	118-135	22-51	349-12	20.2-22.0
7144	01 Jun	185.6	117-134	22-51	88-111	20.1-21.9
7150	02 Jun	186.2	117-133	22-50	56-79	20.0-21.8
7154	03 Jun	186.6	117-132	21-49	155-177	20.0-21.7
7158	04 Jun	187.1	117-131	21-49	254-276	19.9-21.6
7162	04 Jun	187.5	116-131	20-48	353-15	19.8-21.5
7166	05 Jun	188.0	115-130	19-48	91-113	19.7-21.4
7170	06 Jun	188.3	115-129	19-47	190-211	19.7-21.3
7174	06 Jun	188.8	113-128	18-46	290-310	19.6-21.2
7178	07 Jun	189.2	112-127	18-45	28-49	19.5-21.2
7182	08 Jun	189.6	112-127	17-45	126-148	19.5-21.2
7198	11 Jun	191.4	108-124	15-43	162-182	19.2-20.7
7202	12 Jun	191.8	107-124	15-43	261-281	19.1-20.7
7208	13 Jun	192.4	106-123	14-42	230-250	19.0-20.6
7212	14 Jun	192.9	105-123	13-41	329-348	19.0-20.5
7216	14 Jun	193.3	104-122	13-41	67-87	18.9-20.4
7222	15 Jun	194.0	103-121	12-40	36-55	18.8-20.3
7226	16 Jun	194.4	102-120	11-39	135-154	18.7-20.2
7230	17 Jun	194.8	101-120	11-39	235-253	18.6-20.1
7234	18 Jun	195.3	99-119	10-38	333-352	18.6-20.1
7238	18 Jun	195.7	98-118	10-37	72-91	18.5-20.0
7244	19 Jun	196.4	97-117	10-37	41-59	18.4-19.9
7248	20 Jun	196.8	96-116	8-36	139-158	18.3-19.8
7252	21 Jun	197.2	95-115	8-36	239-257	18.2-19.7
7256	22 Jun	197.7	93-115	7-35	338-357	18.2-19.6

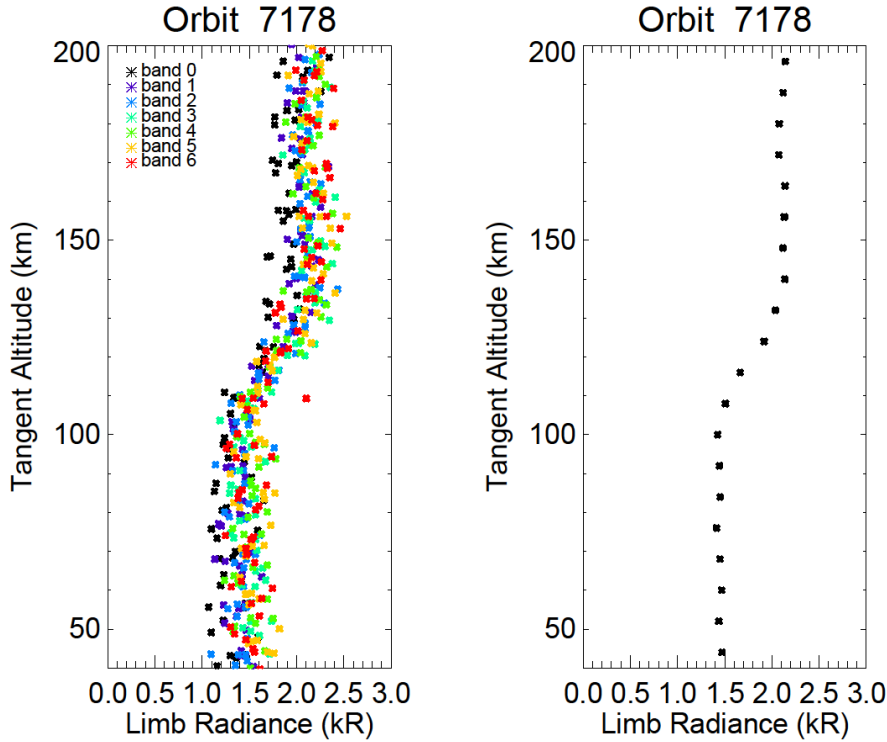
77 *Table 1 : MAVEN orbits used for this study (column 1). The spatial/temporal information for*
78 *each orbits are also given. Solar Zenith Angla (SZA), latitude, East longitude and local time*

79 *range refers to the tangent point of the different lines of sight. The MAVEN orbits drift in*
80 *longitude by $\sim 115^\circ$ /orbit due to the Martian rotation.*

81

82 The spacecraft altitude varies between 2100 to 3400 km during these 6 inbound limb
83 observations. During these observations, the approximate distance between the spacecraft and the
84 tangent point is ~ 5000 km. The IUVS slit projection is normal to the orbit of MAVEN
85 (perpendicular to the vertical direction). The IUVS spatial bins (corresponding to a binning of
86 115 physical pixels along the slit) projection at the tangent point is ~ 20 km.

87 The 42 individual limb profiles for orbit #7178 are displayed in Figure 2. For all the orbits, the
88 variations of the brightness between the different limb scans (~ 0.14 kR) is close to the error bar
89 of the individual measurement (~ 0.13 kR). There are small variations of sensitivity between the
90 different spatial bins along the slit, but we do not apply any flatfield corrections in this study,
91 because our results are not sensitive to the absolute sensitivity of the spatial bins. We average the
92 profiles to increase the signal to noise. Profiles are averaged every 8 km. The average profile is
93 shown in Figure. 2.



94

95 *Figure. 2 : Left : Vertical profiles of the H Lyman- α brightness measured at limb between 40 and*
 96 *200 km for each of 7 spatial bins (labeled as “bands” and shown with different colors) during*
 97 *orbit 7178 for all six inbound limb scans, observed on 7 June 2018. The error bar for each*
 98 *individual value is ~ 0.13 kR. Right : Average profile derived with a vertical resolution of 8 km.*
 99 *The uncertainty on the mean is ~ 0.03 kR, lower than the thickness of the points.*

100

101 The brightness between 160 and 200 km is approximately constant in the profiles shown in
 102 Figure 2. The brightness between 40 and 80 km is also constant. The vertical variation of the
 103 brightness is well described by the formulation in Equation 1 (see Chaufray et al., 2011):

$$104 \quad I(z) = I_0 + (I_1 - I_0) \exp(-\tau_{CO_2}(z)) \quad (1)$$

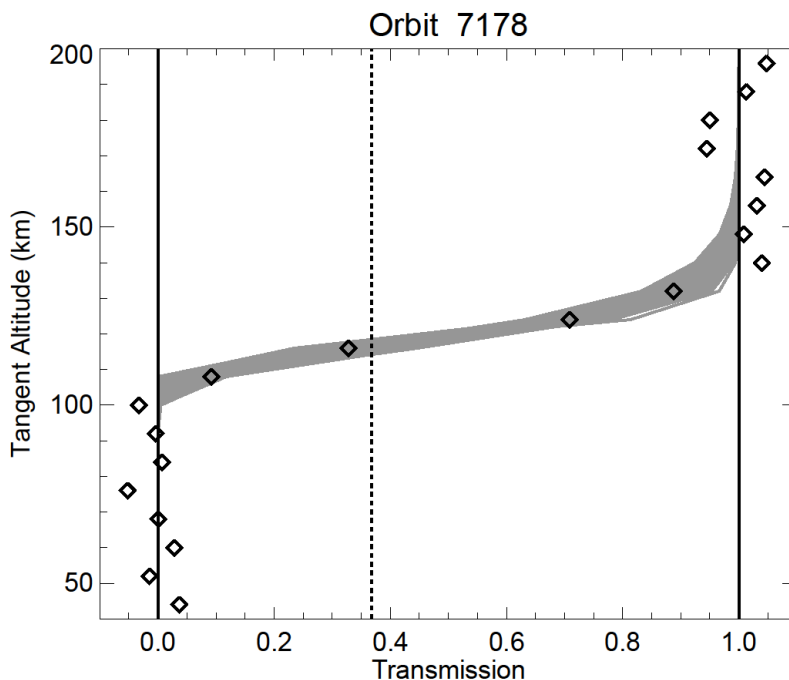
105 where $\tau_{CO_2}(z)$ is the slant path integrated atmospheric transmittance by CO_2 at tangent altitude z ,
 106 I_0 is the average brightness between 40 and 80 km, I_1 is the average brightness between 160 and
 107 200 km. I_0 corresponds to Lyman- α photons emitted between the spacecraft and the absorption
 108 layer, i.e. the region below 100 km, $I_1 - I_0$ corresponds to the contribution of photons mostly
 109 emitted above the absorption layer, in the solar illuminated side of the line of sight . These

110 photons are absorbed or “occulted” by the atmospheric CO₂ for z lower than 100 km (where τ_{CO_2}
 111 $\gg 1$), not absorbed for $z > 160$ km (where $\tau_{\text{CO}_2} \ll 1$), and partly absorbed in between.

112 For each observation, a normalized brightness or transmission function (Equation 2) can be
 113 deduced. As the transmission function computed from stellar occultation (e.g. Quémerais et al.
 114 2006), this function is independent of the absolute calibration of the instrument as long as the
 115 sensitivity doesn’t drift over time of the observation.

$$116 \quad T(z) = \frac{I(z) - I_0}{I_1 - I_0} = e^{-\tau_{\text{CO}_2}} \quad (2)$$

117 An example of transmission function is displayed in Figure 3 for orbit #7178



118
 119 *Fig. 3 Transmission function for orbit 7178 (diamonds) and the best fit derived using a function*
 120 *given by Eq. 3 (solid line). The two vertical solid lines indicate Transmission= 0 and*
 121 *Transmission =1. The vertical dotted line indicate Transmission = e^{-1} . Because I_0 and I_1 are*
 122 *average values between 40-80 km and 160-200 km respectively, the computed individual*
 123 *transmission values can be < 0 (when $I(z) < I_0$) near 100 km and > 1 (when $I(z) > I_1$) near 160*
 124 *km respectively. The best fits obtained from a Monte Carlo error analysis are also displayed by*
 125 *the grey area.*

126

127 A theoretical expression of the CO₂ absorption optical thickness can be derived assuming an
 128 isothermal absorption layer between 100 and 160 km (Equation 3).

$$129 \quad \tau_{CO_2}(z) = n(z)H\sqrt{\frac{2\pi R}{H}}\sigma = n(z_0)H\sqrt{\frac{2\pi R}{H}}\sigma \exp\left[-\frac{(z-z_0)}{H}\right] \quad (3)$$

130 The isothermal assumption is justified at the nightside, given the limited accuracy of the method.
 131 In Equation 3, $n(z)$ is the CO₂ density at the tangent point altitude z , H the scale height of the CO₂
 132 density, σ is the CO₂ absorption cross section at 121.6 nm (equal to 6.2×10^{-20} cm²), the product
 133 $n(z)H$ is the column density above z and the factor $(2\pi R/H)^{1/2}$ is the approximate ratio of the limb
 134 length and the vertical length for a spherically symmetric atmosphere around the tangent point,
 135 where R is the Martian radius. $n(z_0)$ is the density at an arbitrary reference altitude z_0 .

136 We assume the absorption cross section is independent on the temperature. The CO₂ cross section
 137 at Lyman-alpha for $T=195$ K and $T=295$ K can be found in Qu  merais et al. 2006 (Fig. 17). At
 138 121.6 nm, the relative difference is small $\sim 0.2\%$, so we could expect a small effect on our results
 139 compared to other source of uncertainties.

140 This relation shows that the expected transmission function can be fitted by a function given by

$$141 \quad f(z) = \exp\left\{-A\sqrt{H} \exp\left[-\frac{(z-z_0)}{H}\right]\right\} \quad (4)$$

142 A and z_0 are not independent, and therefore z_0 can be fixed arbitrarily (here to 110 km) without
 143 losing generality. Changing z_0 will provide exactly the same fit, since A would be adjusted to
 144 produce the same transmission function.

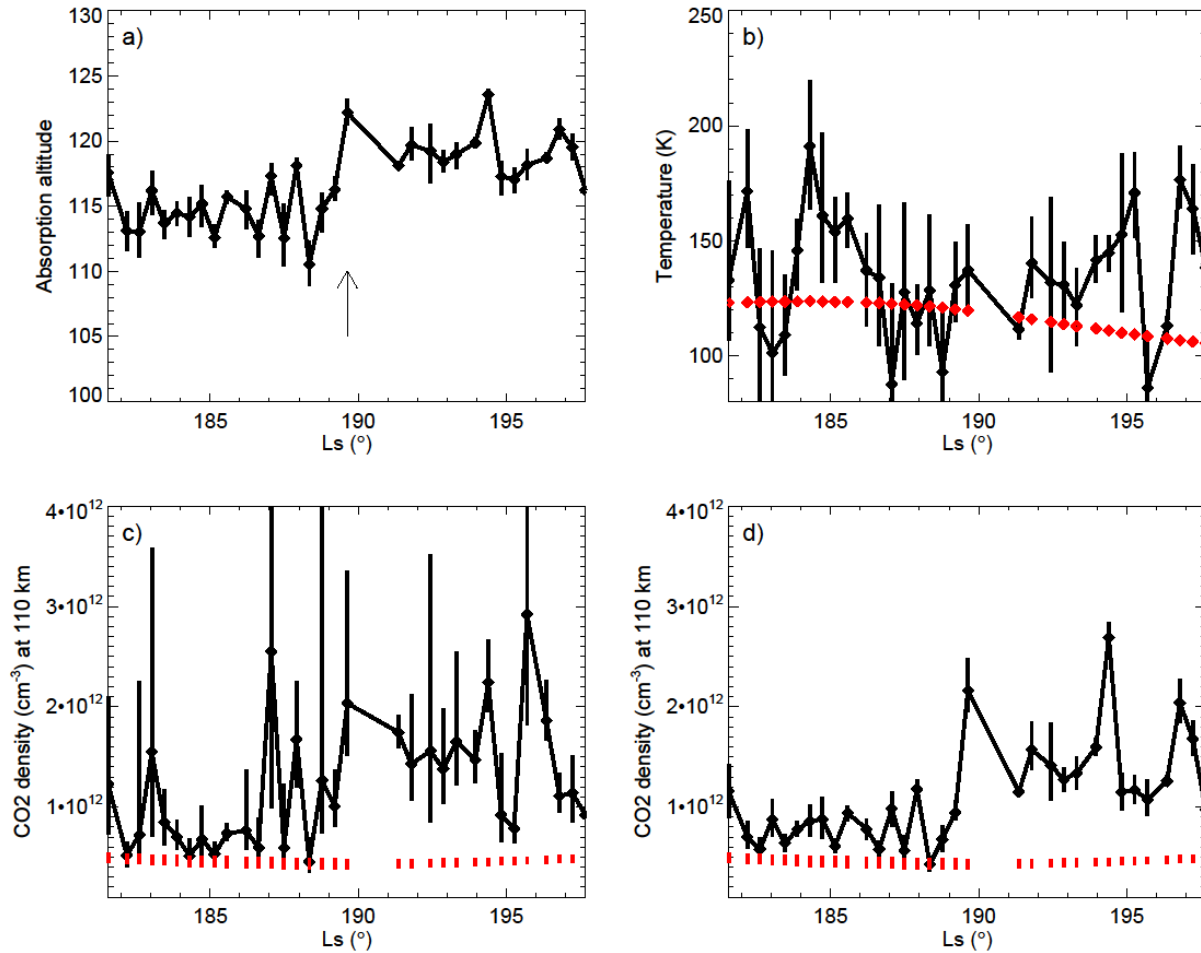
145 From A we can derive the CO₂ density at z_0 , and from H we can derive the average temperature
 146 of the 100 – 160 km layer and above.

147 We use a Levenberg-Marquardt fit, using the IDL fit package from Markwardt (2009) to derive
148 the best fit of the observed transmission functions for each of the 33 orbits. For each orbit, we
149 perform a Monte Carlo error analysis by adding a random noise to the observed transmission,
150 following a gaussian law $\exp(-\delta T^2/2\sigma^2)$ where σ is the standard deviation on the transmission
151 between 40 – 80 km (~ 0.05). From 1000 random profiles, we derive the values of the two free
152 parameters with the fit procedure described above. The 1000 best fits of the transmission
153 obtained for orbit 7178 are shown in Fig. 3. From this sample, the median, first and last deciles of
154 the free parameters are considered as the best fit values, and the uncertainties on the parameters.
155 For each orbit, the altitude z where $\tau_{CO_2} = 1$ (corresponding to a slant CO_2 density of $1.6 \times 10^{19} \text{ cm}^{-2}$)
156 can therefore be calculated.

157 To estimate the uncertainty associated to the non_isothermal assumption, we have numerically
158 computed the transmission function for non isothermal cases using the temperature profiles from
159 the Mars Climate Database (MCD) or from Groller et al. (2018). We then applied the same
160 retrieval method to the computed transmission function. The uncertainty on the altitude where $\tau =$
161 1 due to the non-isothermal assumption is estimated to be lower than 2 km.

162 **3) Results**

163 The altitude where CO_2 optical thickness is equal to 1 and the temperature of the absorption layer
164 are displayed in Figure 4. The CO_2 density at 110 km derived from the best fit temperature as
165 well as from an assumed constant temperature of 135 K for all observations are also shown.



166
 167 *Fig. 4 a) Variations of the CO₂ absorption altitude (km), defined as the altitude where the slant*
 168 *CO₂ absorption optical thickness at Lyman- α is equal to 1 with the solar longitude Ls. b) derived*
 169 *temperature for each orbit from the CO₂ scale height. c) variations of the CO₂ density with Ls*
 170 *considering the temperature derived from the fit. d) Same as c) but using a same temperature of*
 171 *135 K for the full period. The range of temperature and CO₂ density at 110 km extracted from the*
 172 *Mars Climate Database at the same position are shown by red lines for panels 3b, 3c and 3d. The*
 173 *arrow on panel 3a indicate the time of orbit #7182.*

174 The altitude where the CO₂ optical thickness is equal to 1 is almost constant before orbit #7182
 175 (114.5 km with a standard deviation of 2 km) and increases to 119.0 km (standard deviation of 2
 176 km) for the period starting with orbit 7182. The uncertainty on the mean value is 0.5 km for both
 177 periods. Orbit 7182 occurred on 8 of June 2018 corresponding to the time where the increase of
 178 the dayside CO₂ density at 150 km was observed from the navigation camera (NAVCAM) of

179 MAVEN (Bougher et al., 2019) and IUVS dayglow emissions (Jain et al., this issue). This
180 increase is associated with the heating of the lower atmosphere by the global dust storm.

181 The derived temperature is within the range expected for the deep nightside thermosphere (e.g.
182 Forget et al. 2009, Gröller et al. 2018). The derived uncertainties are $\sim 30\text{K}$ and are consistent
183 with the range of temperature variations derived from stellar occultations (Forget et al. 2009,
184 Groller et al 2018). The average temperature derived from the full set of observations is 135 K
185 with a standard deviation of 25 K similar to the uncertainty derived from the fits. The average
186 temperature before orbit 7182 is 133K with a standard deviation of 28K and for the period
187 starting with orbit 7182, the average value is 136K with a standard deviation of 23 K . This
188 variation seems different from the temperature decrease predicted by the MCD. Given the large
189 uncertainty on the derived temperature it is not possible to attribute this difference to the global
190 dust storm. It is not possible from our observations to conclude if the orbit to orbit variations of
191 the temperature is real because the temporal variation of the derived temperature is not different
192 from the derived error bar. We also fit the transmission function for each observation using the
193 value of the average temperature to derive the CO_2 density variations at 110 km (Fig. 4d). In this
194 case, the CO_2 density variations show an increase by a factor $\sim 1.9\pm 0.2$ after orbit #7178. The
195 average density calculated from all orbits before orbit 7182 is $7.8\times 10^{11}\text{ cm}^{-3}$ and the standard
196 deviation is $2.0\times 10^{11}\text{ cm}^{-3}$ ($5.8\pm 1.5\times 10^{-8}\text{ kg/m}^3$, assuming a CO_2 mixing ratio of 0.96). It increases
197 to $14.7\pm 4.8\times 10^{11}\text{ cm}^{-3}$ ($11.2\pm 3.6\times 10^{-8}\text{ kg/m}^3$) after orbit 7182, as expected from the increase of
198 the CO_2 absorption layer altitude. CO_2 densities derived before and after 8 of June are in the
199 range of the CO_2 density derived by Forget et al. (2009) near $L_s = 180^\circ$. Using another
200 temperature changes the derived CO_2 density, but the increase factor is only slightly modified.
201 For example, using a temperature of 120 K – close to the derived nightside temperature at 110

202 km obtained from stellar occultations by SPICAM in 2004, 2005 and 2006 (Forget et al. 2009) –
203 we obtain a CO₂ density increase from $9.0 \pm 2.4 \times 10^{11} \text{ cm}^{-3}$ to $18.3 \pm 6.0 \times 10^{11} \text{ cm}^{-3}$.

204 **4) Discussion**

205 A large-scale dust storm was detected in early June by Mars Reconnaissance Orbiter (MRO) Mars
206 Color Imager (MARCI) and Mars Climate Sounder (MCS) instruments. These instruments
207 associated the dust storm with an increase in lower atmospheric temperature (Zurek et al. 2018,
208 Kass et al. 2018). The first sign of this global dust storm was detected by MAVEN on 8 June
209 (orbit #7184) in the dayside thermosphere. MAVEN accelerometers detected an enhancement in
210 dayside CO₂ density at 150 km by a factor ~ 2 (Zurek et al. 2018) in agreement with the density
211 variations observed by the NAVCAM and NGIMS instruments (Elrod et al. this issue, Bougher et
212 al. 2019). From dayglow observations, IUVS observed an increase in the altitude of peak
213 brightness of 5 to 8 km (Jain et al. this issue). This variability is in agreement with the derived
214 variability measured at the nightside for the observations presented in this study.

215 The atmospheric mass density measured by the NAVCAM was $\sim 0.25\text{-}0.3 \text{ kg/km}^3$ at 150 km
216 before the 8 of June and $\sim 0.4\text{-}0.55 \text{ kg/km}^3$ after MAVEN orbit 7184 (Bougher et al., 2019). At
217 such altitudes, assuming a CO₂ mass mixing ratio between 0.7 and 0.9, we convert the
218 atmospheric mass density to CO₂ number density between $2.3 - 3.7 \times 10^9 \text{ cm}^{-3}$ and between 3.8 and
219 $6.8 \times 10^9 \text{ cm}^{-3}$ before and during the dust storm, respectively. To compare these values to the
220 derived values in this study requires extrapolating the density derived at 110 km to 150 km.
221 Assuming an isothermal layer between 110 and 150 km and a temperature of 135 K results in a
222 nightside CO₂ density of $3.2 \times 10^9 \text{ cm}^{-3}$ and $6.1 \times 10^9 \text{ cm}^{-3}$ at 150 km, close to the dayside CO₂
223 density. Considering a temperature of 120 K gives respective CO₂ densities of $2.0 \times 10^9 \text{ cm}^{-3}$ and
224 $4.0 \times 10^9 \text{ cm}^{-3}$, lower than the dayside derived density. However, NAVCAM shows a decrease of

225 the density at 150 km when MAVEN periapsis is moving from the dayside to the nightside
226 (Bougher et al. 2019), and therefore a temperature of 120 K at the nightside between 110 and 150
227 km would provide better agreement between the two sets of observations. A possible bias on our
228 retrieved density is the uncertainty in the tangent altitude due to the uncertainty in the real
229 pointing (Chaufray et al. 2011). During the observations presented above, the typical distance
230 between the spacecraft and the tangent point is ~ 5000 km. The IUVS spatial bins (corresponding
231 to a binning of 115 physical pixels along the slit) projection at the tangent point is large ~ 20 km.
232 A systematic change of ± 10 km on the altitude of the tangent point would increase/decrease all
233 the derived CO₂ densities at 110 km by a factor ~ 4 . But in both cases, the ratio of the density
234 during and before the dust storm would not be modified if these effects are systematic.

235 **5) Summary and conclusion**

236 IUVS observations of the Lyman- α hydrogen line in the Martian lower thermosphere show an
237 increase in the altitude of absorption layer of the Lyman- α emission by CO₂ on 8 June 2018,
238 coincident with the expansion of the dayside thermosphere observed by several MAVEN
239 instruments. This increase is most likely associated with the large-scale dust storm observed by
240 MRO few days before that heated the lower atmosphere. This altitude variation is attributed to an
241 increase of the CO₂ density by a factor $\sim 1.9 \pm 0.2$ assuming an isothermal atmosphere between
242 100 and 160 km. While the absolute derived density is sensitive to the accuracy of the pointing
243 and the assumed temperature, the relative variation in density is not. We can estimate the global
244 heating of the lower atmosphere needed to produce such an increase of the density. Assuming a
245 moderately deep region ($\Delta Z = 50$ km) of uniform heating and a constant surface pressure. The
246 increase of the CO₂ density at 110 km is related to the increase of the vertically average scale
247 height $\langle H \rangle$ by

248
$$\beta = \frac{\langle H \rangle_2}{\langle H \rangle_1} = \frac{1}{1 - \frac{\langle H \rangle_1}{\Delta Z} \ln\left(\frac{n_2}{n_1}\right)}$$
 (5)

249
$$\frac{1}{\langle H \rangle_i} = \frac{1}{\Delta Z} \int_0^{\Delta Z} \frac{dz}{H_i(z)},$$
 (6)

250 where, $H_1(z)$ is the atmospheric scale height at $z < 50$ km before 8 June 2018, $H_2(z)$ the scale
 251 height at $z < 50$ km after 8 June 2018 and n_2/n_1 the observed CO_2 density increase at 110 km,
 252 Assuming $\langle H \rangle_1$ between 8 - 12 km, it leads to an average increase of the temperature between
 253 ~10 - 20% (~25 – 50 K) in the lower atmosphere of Mars. This is just an estimate of the heating.
 254 Simulations from Global Circulation Models, including the dynamics of the atmosphere are
 255 needed to capture the links between the lower atmosphere and the upper atmosphere more
 256 accurately. This analysis confirms the global effect of the GDS on the nightside thermosphere of
 257 Mars at altitudes not sampled by other instruments and will provide additional constraints to
 258 better understand the dynamics and heating distribution associated with such events.

259

260 **Acknowledgments**

261 This work and the MAVEN project are supported by NASA through the Mars Exploration
 262 Program. All IUVS inbound limb (“inlimb”) data used in this paper with revision/version tag
 263 v13_r01 are archived in NASA’s Planetary Data System :

264 http://atmos.nmsu.edu/data_and_services/atmospheres_data/MAVEN/maven_iuvs.html. The
 265 parameters extracted from the MCD v5.3 can be found at [http://www-](http://www-mars.lmd.jussieu.fr/mcd_python/index5.html)
 266 [mars.lmd.jussieu.fr/mcd_python/index5.html](http://www-mars.lmd.jussieu.fr/mcd_python/index5.html).

267 J-Y. Chaufray is supported by the Centre National d'Etudes Spatiales. We thanks two anonymous
268 referees for their constructive comments.

269
270 **References**

271 Bertaux, J-L., F. Leblanc, S. Perrier, E. Quémerais, O. Korablev, E. Dimarellis, A. Réberac, F.
272 Forget, P.C. Simon, S.A. Stern, B. Sandel, and SPICAM team, Nightglow in the upper
273 atmosphere of Mars and implications for atmospheric transport, *Science*, 307, 566-569,
274 (2005)

275 Bougher S.W., R.H. Tolson, R.W. Zurek, D.T. Bairn, R. Lugo, and G. Jenkins, MAVEN
276 Aerobraking campaign of 2019 and the resulting accelerometer measurements : wave
277 features in the Martian thermosphere, DPS-EPSC, 2019

278 Chaufray, J-Y., K.D. Retherford, D.G. Horvath, J-L. Bertaux, F. Forget, and F. Leblanc, The
279 density of the upper martian atmosphere measured by Lyman- α absorption with Mars
280 Express SPICAM, *Icarus*, 215, 522-525, 2011

281 Elrod M. et al., this issue

282 Forget, F., F. Montmessin, J-L. Bertaux, F. Gonzalez-Galindo, S. Lebonnois, E. Quémerais, A.
283 Réberac, E. Dimarellis, and M.A. Lopez-Valverde, Density and temperatures of the upper
284 Martian atmosphere measured by stellar occultations with Mars Express SPICAM.

285 Fox, J., M.I. Galand, and R.E. Johnson, Energy deposition in planetary atmospheres by charged
286 particles and solar photons., *Space Sci. Rev.*, 139, 3-62, (2008)

287 Gröller, H.F., R.V. Yelle, T.T. Koskinen, F. Montmessin, G. Lacombe, N.M. Schneider, J.
288 Deighan, A.I.F Stewart, S.K. Jain, M.S. Chaffin and 9 co-authors, Probing the Martian
289 upper atmosphere with MAVEN/IUVS stellar occultations, *Geophys. Res. Lett*, 42, 9064,
290 (2015)

291 Gröller, H., F. Montmessin, R.V. Yelle, F. Lefèvre, F. Forget, N.M. .Schneider, T.T. Koskinen, J.
292 Deighan, and S.K. Jain, MAVEN/IUVS stellar occultation measurements of Mars
293 atmospheric structure and composition, *J. Geophys. Res.*, 123, 1449-1483, (2018)

294 Jain, S. et al., this issue

295 Kass D.M., A. Kleinboehl, J.H. Shirley, J.T. Schofield, D. McCleese, N.G. Heavens, Overview of
296 the 2018a Global dust event from Mars Climate Sounder Observations, AGU, Fall
297 Meeting 2018, abstract #P34A-02.

298 Markwardt, C. B. 2009, "Non-Linear Least Squares Fitting in IDL with MPFIT," in proc.
299 *Astronomical Data Analysis Software and Systems XVIII*, Quebec, Canada, ASP
300 Conference Series, Vol. 411, eds. D. Bohlender, P. Dowler & D. Durand (Astronomical
301 Society of the Pacific: San Francisco), p. 251-254 (ISBN: 978-1-58381-702-5; [Link to](#)
302 [ASP title listing](#))

303 McClintock, W.E., N.M. Schneider, G.M. Holsclaw, J.T. Clarke, A.C. Hoskins, F. Montmessin,
304 R.V. Yelle, and J. Deighan, The Imaging Ultraviolet Spectrograph (IUVS) for the
305 MAVEN mission, *Space Sci. Rev.*, DOI 10.1007/s11214-014-0098-7, 2015

306 Quémerais, E., J-L. Bertaux, O. Korablev, E. Dimarellis, C. Cot, B. Sandel, and D. Fussen,
307 Stellar occultations observed by SPICAM on Mars Express, *J. Geophys. Res.*, 111,
308 E09S04, doi: 10.1029/2005JE002604, 2006

309 Zurek, R.W., S.W. Bougher, R. Tolson, D. Baird, S. Demcak, D.M. Kass, R. Lugo, and B.M.
310 Jakosky, The Planet-Encircling Dust Storm: Effects on the Mars Upper Atmosphere as
311 seen in MAVEN Accelerometer Data, AGU, Fall Meeting 2018, abstract #P43J-3864

312

313

314

315

316

317

318

319

320

321

322

323

324

325

326

327

328

329

330

331

332

Figure 1.

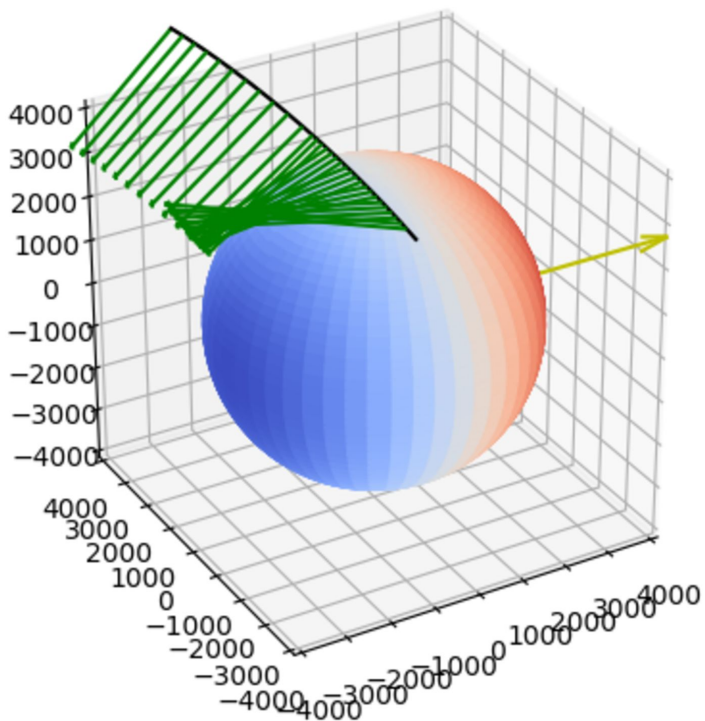
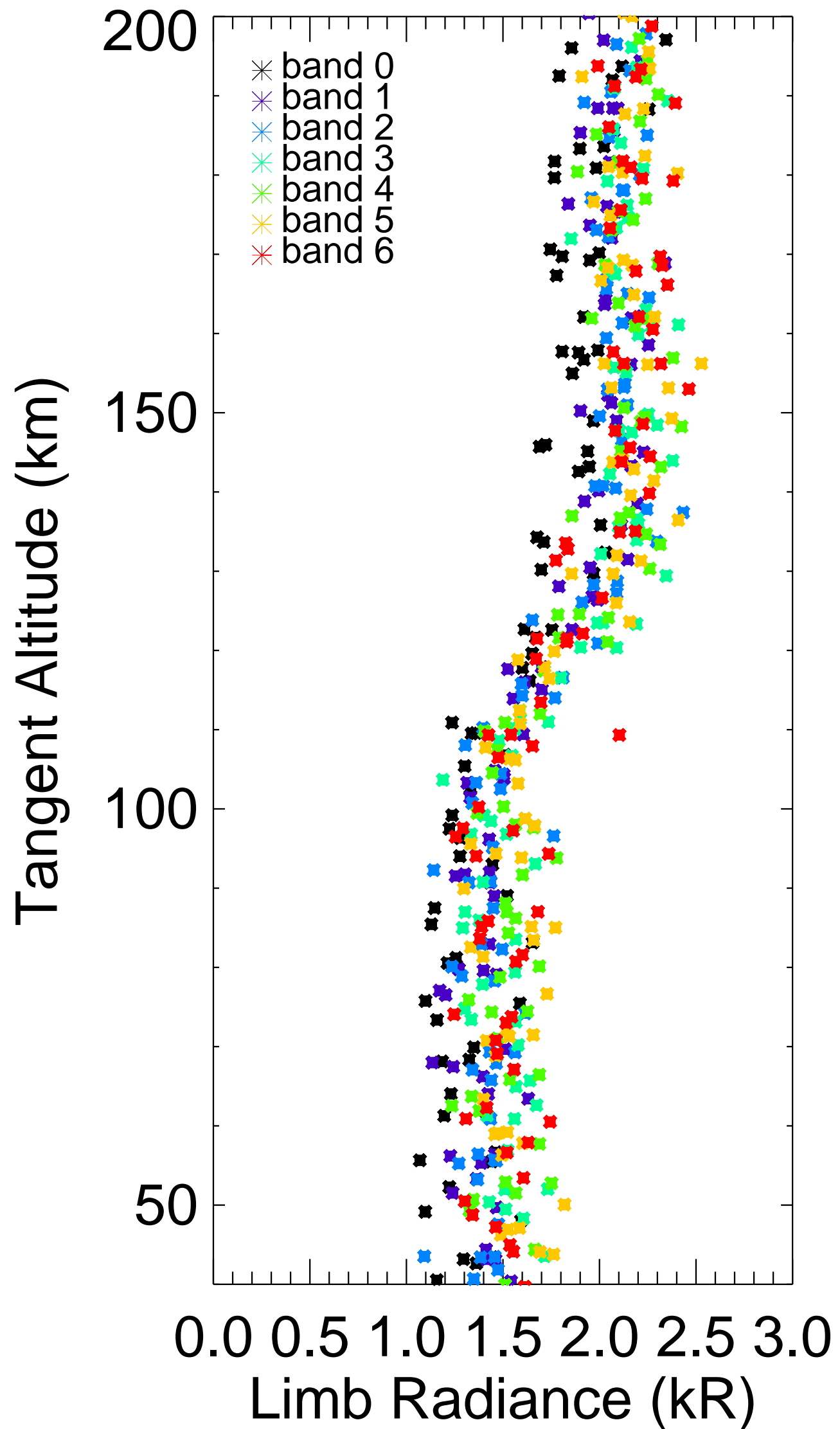


Figure 2.

Orbit 7178



Orbit 7178

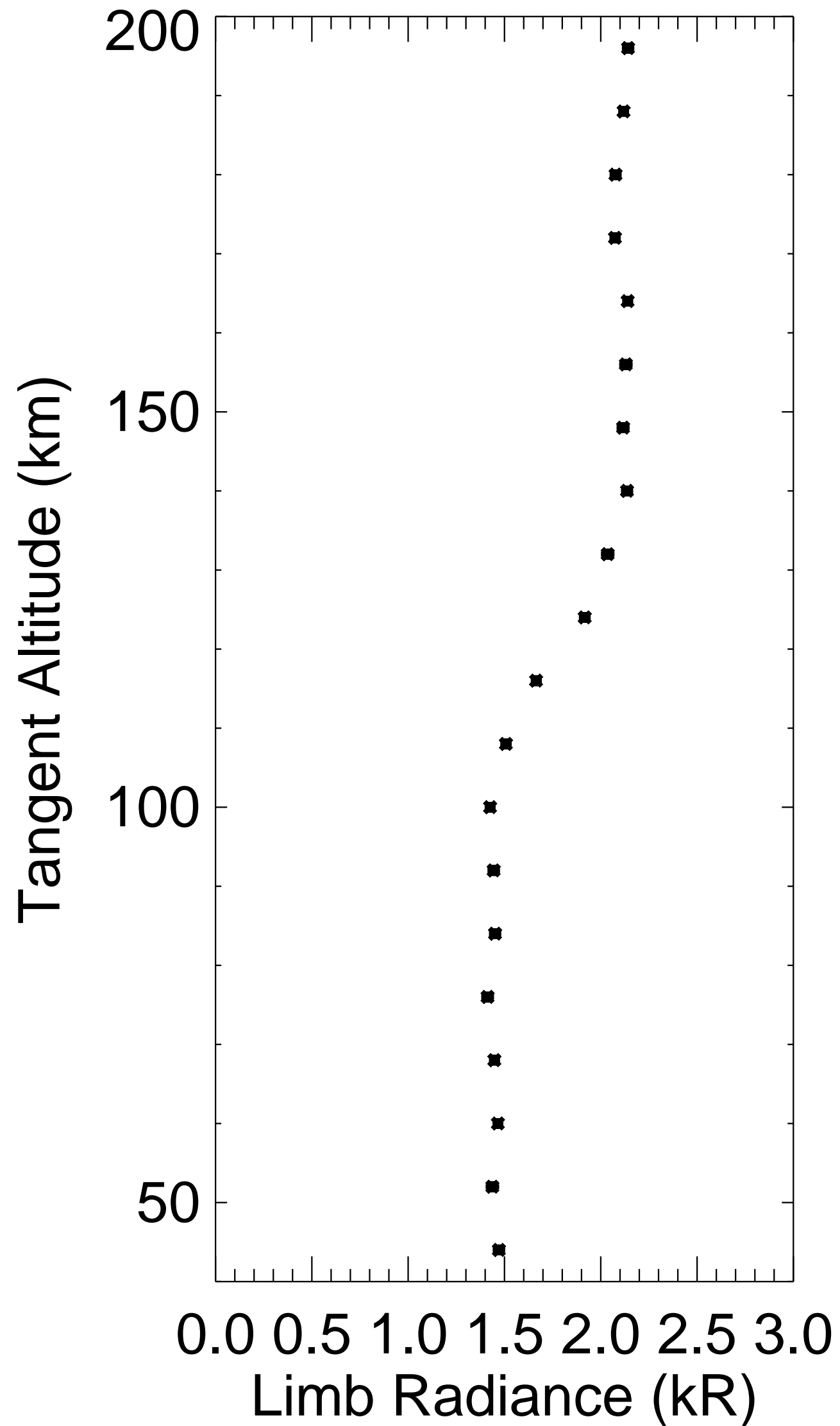


Figure 3.

Orbit 7178

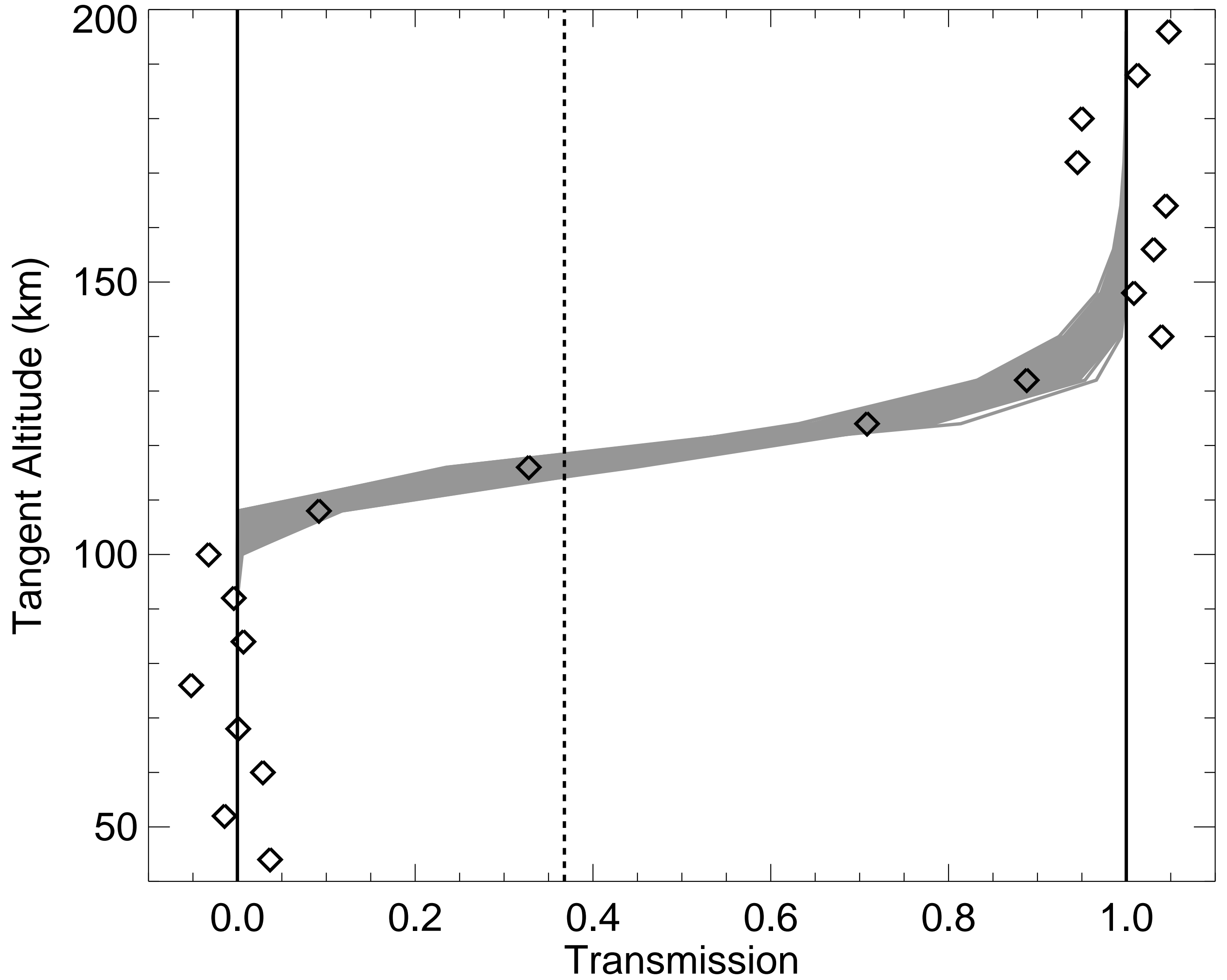


Figure 4.

